The International Journal of Advanced Manufacturing Technology
https://doi.org/10.1007/s00170-026-18207-1

ORIGINAL ARTICLE

Effect of oscillation process parameters in direct laser metal deposition 3d printing deposition for single layer track using Ti-6al-4v: microhardness analysis

Jailani Jamaludin[1,2,3] · Mohd Azlan Suhaimi[3] · Safian Sharif[3] · Yusuf Kaynak[4] · Abdul Hamid Ahmad[3]

Received: 13 April 2025 / Accepted: 21 April 2026
© The Author(s) 2026

Abstract
This study focuses on optimizing Direct Laser Metal Deposition (DLMD) process parameters to enhance microhardness in single layer tracks using Ti-6Al-4V materials for powder and substrate. However, achieving consistent and high microhardness remains challenging. Using the Taguchi method and ANOVA, the optimal oscillation parameters were identified as 70% overlap (OL) and 800 mm/min travel rate (RV). These parameters significantly improved microhardness, particularly in the top and middle deposition regions. High microhardness in these layers enhances wear resistance and structural durability, which are critical for the long-term performance of DLMD's fabricated components. Signal-to-noise ratio analysis confirmed RV as the dominant factor, influencing thermal gradients and solidification behavior. Microscopic analysis reveals distinct microstructures, including equiaxed grains at the top, cellular structures in the middle, and columnar grains near the substrate, attributed to varying cooling rates and thermal gradients. Regression models further clarify the relationship between process parameters and microhardness. The findings represent an initial parameter screening under fixed conditions, providing preliminary guidance for optimizing DLMD processes toward improved material properties, stability and manufacturing precision.

Keywords Direct laser metal deposition (DLMD) · Additive manufacturing (AM) · Ti-6Al-4V · Parameters optimization · Microhardness

1 Introduction

One of the most transformative applications of machine tools is additive manufacturing (AM), commonly referred to as 3D printing. This innovative technique, which creates physical objects through the incremental addition of material based on geometrical models, is revolutionizing the way components are designed and fabricated [1–3]. AM encompasses several methods tailored to specific production needs and is broadly categorized into seven primary processes: binder jetting (BJT), directed energy deposition (DED), material extrusion (MEX), material jetting (MJT), powder bed fusion (PBF), sheet lamination (SHL), and vat photopolymerization (VPP) [4]. Among these methods, BJT, DED, and PBF are particularly significant for manufacturing metal components. Directed Energy Deposition (DED) stands out for its ability to directly fabricate intricate 3D shapes from digital designs, distinguishing it from conventional techniques like welding and cladding. A notable variant of DED is Direct Laser Metal Deposition (DLMD). Figure1 provides a visual representation of the DLMD process. The process employs a laser as a focused heat source to melt and deposit metal powder, forming complex structures.

✉ Jailani Jamaludin
jailani.j@uow.edu.my

1 School of Engineering, University of Wollongong Malaysia, Glenmarie Campus, Jalan Kontraktor U1/14, Glenpark U1, Shah Alam 40150, Malaysia

2 School of Engineering, UOW Malaysia KDU Penang University College, Lebuhraya Bandar Cassia, Batu Kawan, Pulau Pinang 14100, Malaysia

3 Faculty of Mechanical Engineering, Universiti Teknologi Malaysia, Johor Bahru 81310, Johor, Malaysia

4 Department of Design and Manufacturing, Faculty of Technology, Mechanical Engineering, Marmara University, Istanbul, Turkey

Published online: 09 May 2026

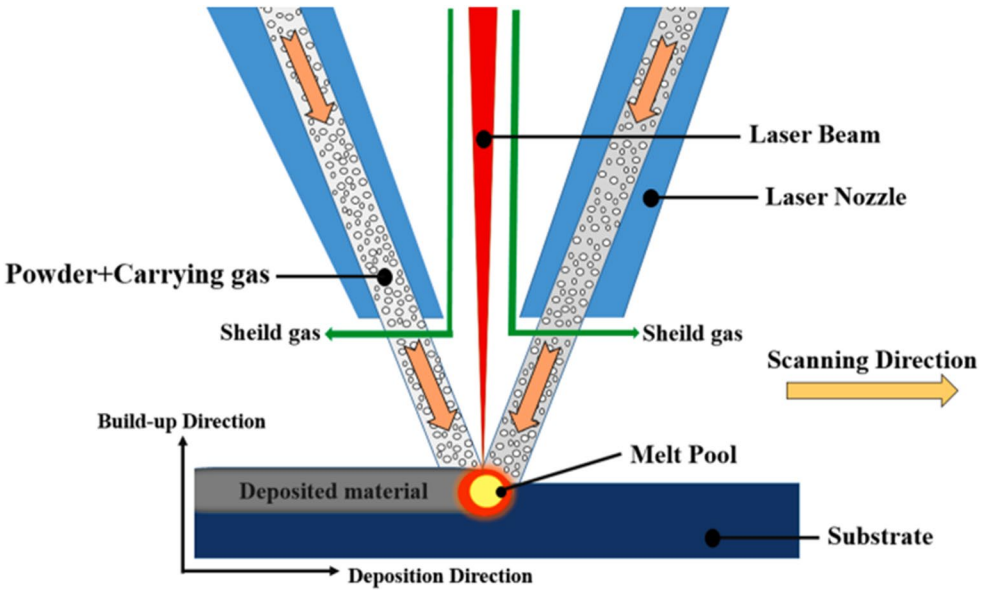


Fig. 1 Schematic diagram for DLMD process [5]

Extensive research has established the suitability of DLMD for manufacturing, with studies highlighting its potential in producing components with superior mechanical properties [5–9]. Prior investigations into DLMD using Ti-6Al-4 V have explored the influence of laser power, scanning speed, and powder feed rate on microstructure and hardness [10–12]. However, many of these studies focus on bulk deposition or multi-layer tracks, with limited emphasis on single-layer oscillation strategies and localized microhardness variation. Microhardness remains a critical performance metric, yet previous works [13–17] often report inconsistent values across deposition regions due to uncontrolled thermal gradients and melt pool dynamics. This study addresses these gaps by introducing a controlled oscillation strategy and systematically analyzing overlap and travel rate effects on microhardness distribution. By focusing on single-layer tracks and applying Taguchi and ANOVA methods, this research offers initial parameter screening, enabling more predictable and vigorous hardness profiles especially in the top regions where wear resistance is most critical.

DLMD systems can be tailored to specific applications through three primary mechanisms. First mechanism is laser condition and material feeding, where the laser beam melts and deposits powder onto the substrate. Second mechanism is melt-pool formation which involving the generation of molten material by the laser and third mechanism is solidification, where the molten material cools and solidifies into the final structure [18, 19]. These mechanisms also have been thoroughly explored in prior research [20]. The versatility of DLMD extends to various metals, including Inconel, stainless steel, tool steel, titanium alloys, chromium, and tungsten [9, 10, 21–29]. However, different materials introduce challenges, such as variations in mechanical properties [12, 26, 30, 31], microstructural characteristics [7, 32, 33], surface roughness [19, 34, 35], and defect formation [36–38]. Recent advancements have emphasized the potential of DLMD for part repair, particularly in the aerospace industry where using of Ti-6Al-4 V in component repair, highlighting its mechanical properties, especially at material interfaces, and its promise for both part repair and full-component manufacturing [11, 39]. Despite the versatility and advantages of DLMD in fabricating metal components, achieving consistent and high microhardness remains a significant challenge. This study aims to optimize oscillation process parameters, specifically overlap value and travel speed, to enhance the microhardness of deposition layers, ensuring improved robustness, stability, and performance.

2 Methodology

The necessary parameters for producing the deposition part were identified, with key benchmarks including scanning speed, powder delivery rate, and laser power. Subsequently, parameters related to oscillation motion, such as overlap values and travel speed, were configured to achieve the desired outcomes. Motion control was based on the traversal movement of the deposition head, and the input parameters were categorized into three distinct levels. To analyze the effects of these input parameters on the output parameters, a series of nine experiments were conducted. The output parameters measured microstructural response such as microhardness of a single-layer track. Table 1 provides a detailed overview of the experimental conditions.

Table 1 Oscillation parameters with design levels

Factors	Acronym	Unit	Level
Overlapping values	OL	%	50 / 70 / 90
Rate of travel speed	RV	mm/min	100 / 450 / 800

Table 2 Composition of powder Ti-6Al-4 V

Factors	Weight%	Weight% σ	Atomic %
Aluminium	5.247	0.264	8.975
Titanium	90.206	0.600	86.907
Vanadium	4.547	0.570	4.119

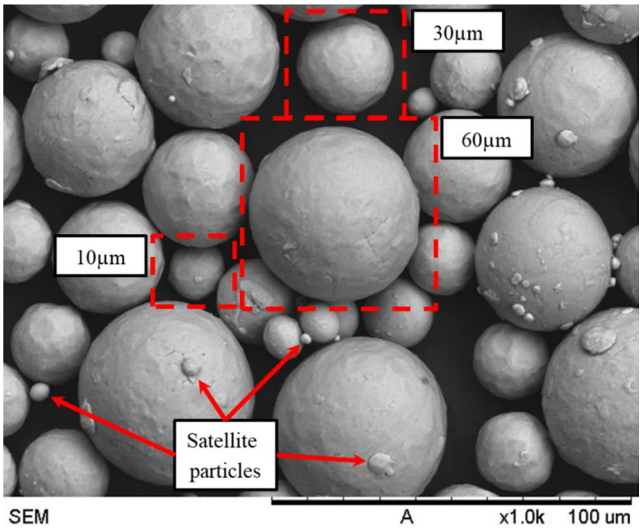


Fig. 2 SEM image of Ti-6Al-4 V powder particles

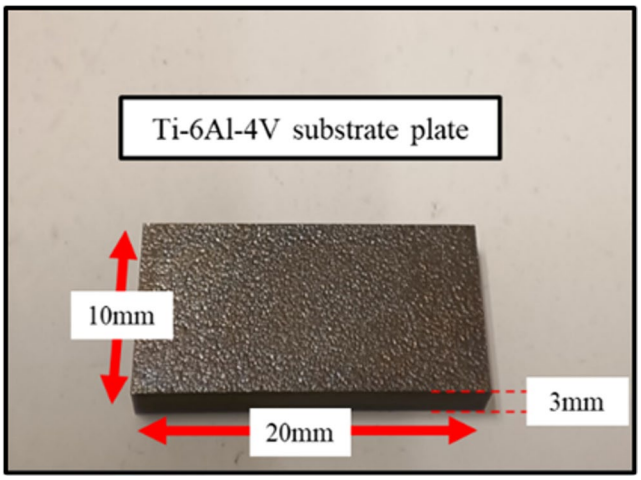


Fig. 3 Image of Ti-6Al-4 V substrate plate

On the materials side, Ti-6Al-4 V powder particles were deposited onto a 10 mm x 20 mm x 3 mm Ti-6Al-4 V plate using the DLMD process. The elemental composition and morphology of the powder particles were examined with a scanning electron microscope (Hitachi S-3400 N). Table 2 details the composition of the Ti-6Al-4 V powder.

Table 3 Fixed factors variable

Variables	Unit	Value
Laser power	W	450
Laser spot diameter	mm	3
Laser focal distance	mm	15
Laser focal length	mm	300
Laser wavelength	nm	1080
Powder particle size	µm	10–60
Powder deposition rate	g/min	3.5
Substrate dimension	mm	10 × 20 × 3
Argon gas flow rate (Shielding)	litre/min	10
Argon gas flow rate (Carrier)	litre/min	3

Figure 2 shows the SEM images of the powder morphology used in the experiment. The powder was produced via the gas atomization method, resulting in spherical particles with some satellite formations on their surfaces. Particle sizes ranged from 10 to 60 µm. The substrate, prepared using wire cut Electrical Discharge Machining (EDM), measured 20 mm x 10 mm x 3 mm as shown in Fig. 3.

For the DLMD process, a 1.5 kW fiber laser equipped with a laser cladding head (LT-CH002A) was employed, featuring a 3 mm spot size, a focal position 15 mm vertically, and a 50 mm clear aperture. A coaxial nozzle design ensured even spray onto the substrate [40]. The powder particles were directed from three annular channels into the powder concentration zone, identified between 15 mm until 20 mm below the nozzle. The cladding head, paired with a Raycus model RFL-C1500X laser fiber power supply, operated at a wavelength of 1080 nm in continuous wave mode. Table3 provides a summary of all the fixed factors used.

The laser parameters (450 W power and 15 mm focal distance) were selected based on preliminary trials and literature benchmarks for Ti-6Al-4 V deposition. These settings ensured sufficient energy density for stable melt pool formation without excessive dilution or thermal distortion. The continuous wave mode provided consistent energy delivery, supporting uniform deposition across the single-layer track. Preliminary results indicate successful deposition for the single layer track using 450 W of laser power, a scanning speed of 100 mm/min, and a powder deposition rate of 3.5 g/min. Building on these results, an oscillation strategy was introduced. For oscillation parameters, the overlap value (OL) and travel rate (RV) were chosen to modulate heat input and cooling rate (Refer Table 1). The overlap ensures sufficient material consolidation and minimizing excessive heat accumulation while travel rate promotes rapid solidification, enhancing microhardness through refined grain structures. These values were validated through Taguchi and ANOVA analysis, confirming their significance in improving layer hardness.

Figure 4 illustrates the oscillation pattern path utilized in the experiment. The overlap is determined by the distance

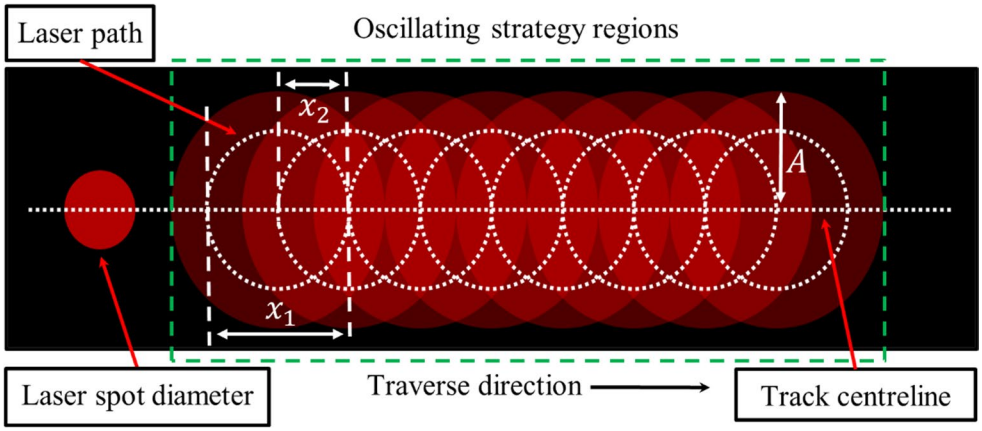


Fig. 4 Oscillation pattern strategy

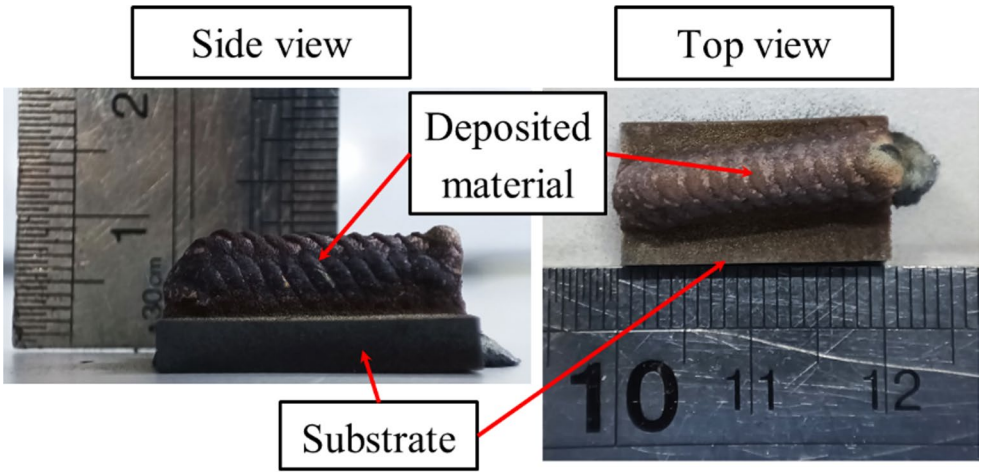


Fig. 5 AM sample with side view and top view

covered from the centerline of the laser's circular motion to the subsequent circles [41, 42]. The value for overlap is calculated using Eq.1 below.

$$\mathrm{OL} = \frac{x_2}{x_1} \times 100 \tag{1}$$

The path of the circular motion is measured from the center of the spot size diameter, specified as 3 mm according to the laser specifications, while the amplitude is measured from the center path to the maximum distance of the track centerline. The overlap value represents the percentage of the circular track diameter and the distance covered by the intersection of consecutive circular tracks. Since the oscillation strategy utilizes circular motion, the deposition rate is influenced by the speed of this motion. One sample was prepared for each experimental setting, and each was analyzed using the same technique to ensure consistent results.

The DLMD process sample was bisected and mounted in resin. The sample then underwent surface preparation by grinding process using 600, 1200, and 2000 grit papers, followed by polishing with a cloth pad before etching to eliminate surface irregularities and ensure accurate microhardness readings. Inadequate preparation can introduce measurement artifacts due to residual stress or uneven indentation surfaces. Microscopic images were captured using an optical microscope (XOPTRON XST150), and SEM images were taken with a scanning electron microscope (Hitachi S-3400 N). Figure 5 shows the printed AM sample using DLMD in both side and top views.

The microhardness test was performed using a Vickers hardness machine (DVK-2 from Matsuzawa Seiki Co. Ltd.), following Vickers standards, with a load of 1000 g and a dwell time of 30 s. Microhardness indentations were made in three regions: top, middle, and substrate below deposition, with three indentations per region and a distance of 10 µm between indentations. The average microhardness of the sample was calculated, as the hardness values determine the mechanical properties of the deposition and substrate, which can be analyzed and observed to evaluate the performance of the DLMD process. Figure 6 displays the cross-sectioned area of the AM sample.

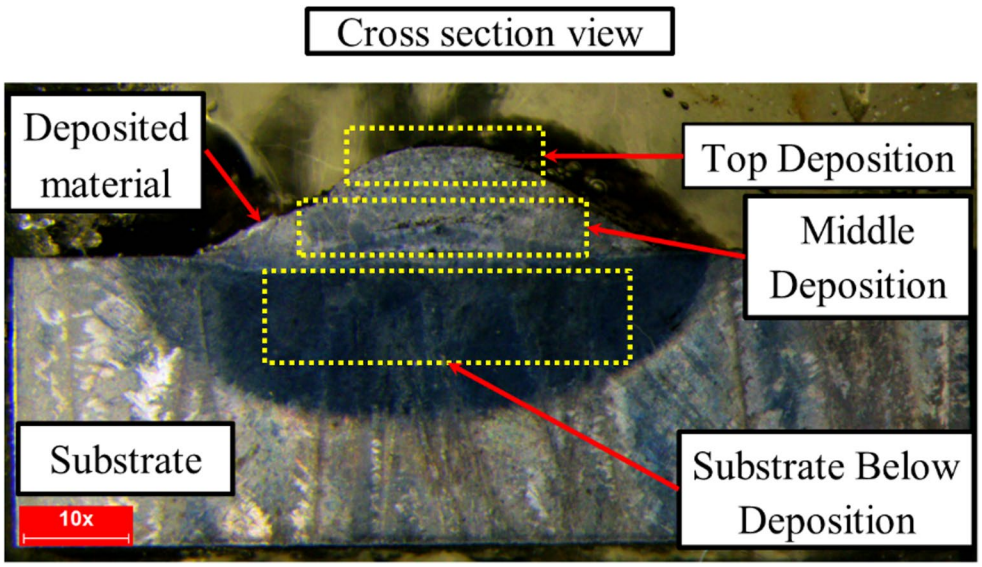


Fig. 6 Area of microhardness testing in cross section view of the AM sample

Table 4 Results overview

No.	Input parameters		Output response		
	OL values(%)	RV (mm/min)	Average Microhardness (HV)		
			Top region	Middle region	Substrate region
1	50	100	366.57	385.03	302.33
2	50	450	361.93	262.27	257.23
3	50	800	447.00	404.77	309.43
4	70	100	382.40	350.00	254.67
5	70	450	425.33	460.13	328.77
6	90	800	407.63	393.97	386.40
7	90	100	298.80	275.80	341.90
8	90	450	407.73	394.87	318.60
9	90	800	401.60	406.77	316.90

3 Results and discussions

The average microhardness for each region of the AM sample was tabulated in Table 4. All output results from the experimental design were analyzed using the Taguchi method for process optimization. Further investigation was conducted using ANOVA, and regression equations for each output were illustrated separately.

The optimization objective in this study was to maximize microhardness at the top deposition layer while ensuring stability across middle and substrate layers. Signal-to-Noise (S/N) ratios were calculated using the Taguchi "larger-the-better" criterion. The example of the calculation as follow:

Formula for (larger-the-better):

$$S/N = -10 \cdot \log_{10}\left(\frac{1}{n}\sum_{i=1}^{n}\frac{1}{y_i^2}\right) \tag{2}$$

where,

$n = 3$ (three runs at OL = 70%).

y_i = hardness values (HV).

calculation for three run which involve the 70% OL, run 4,5 and 6.

$$y_1 = 382.40 \quad \frac{1}{382.40^2} \approx 6.83 \times 10^{-6} \tag{3}$$

$$y_2 = 425.33 \quad \frac{1}{425.33^2} \approx 5.53 \times 10^{-6} \tag{4}$$

$$y_3 = 407.63 \quad \frac{1}{407.63^2} \approx 6.02 \times 10^{-6} \tag{5}$$

sum and average for those three runs.

$$\sum \frac{1}{y_i^2} = 6.83 \times 10^{-6} + 5.53 \times 10^{-6} + 6.02 \times 10^{-6} = 1.84 \times 10^{-5} \tag{6}$$

$$\frac{1}{n}\sum \frac{1}{y_i^2} = \frac{1.84 \times 10^{-5}}{3} = 6.13 \times 10^{-6} \tag{7}$$

log transformation and final results.

$$-10 \cdot \log_{10}(6.13 \times 10^{-6}) = 52.1\,\text{dB} \tag{8}$$

The S/N ratio example demonstrates the calculation for single runs. The full set of results was subsequently tabulated for clarity. Figure 7 indicate three main effect plots for SN ratio of each region separately.

The analysis of the top deposition reveals for the overlap value at 70% achieves the highest SN ratio of 52.1, indicating its stable performance. Similarly, for the rate of travel, at 800 mm/min exhibits the highest SN ratio of

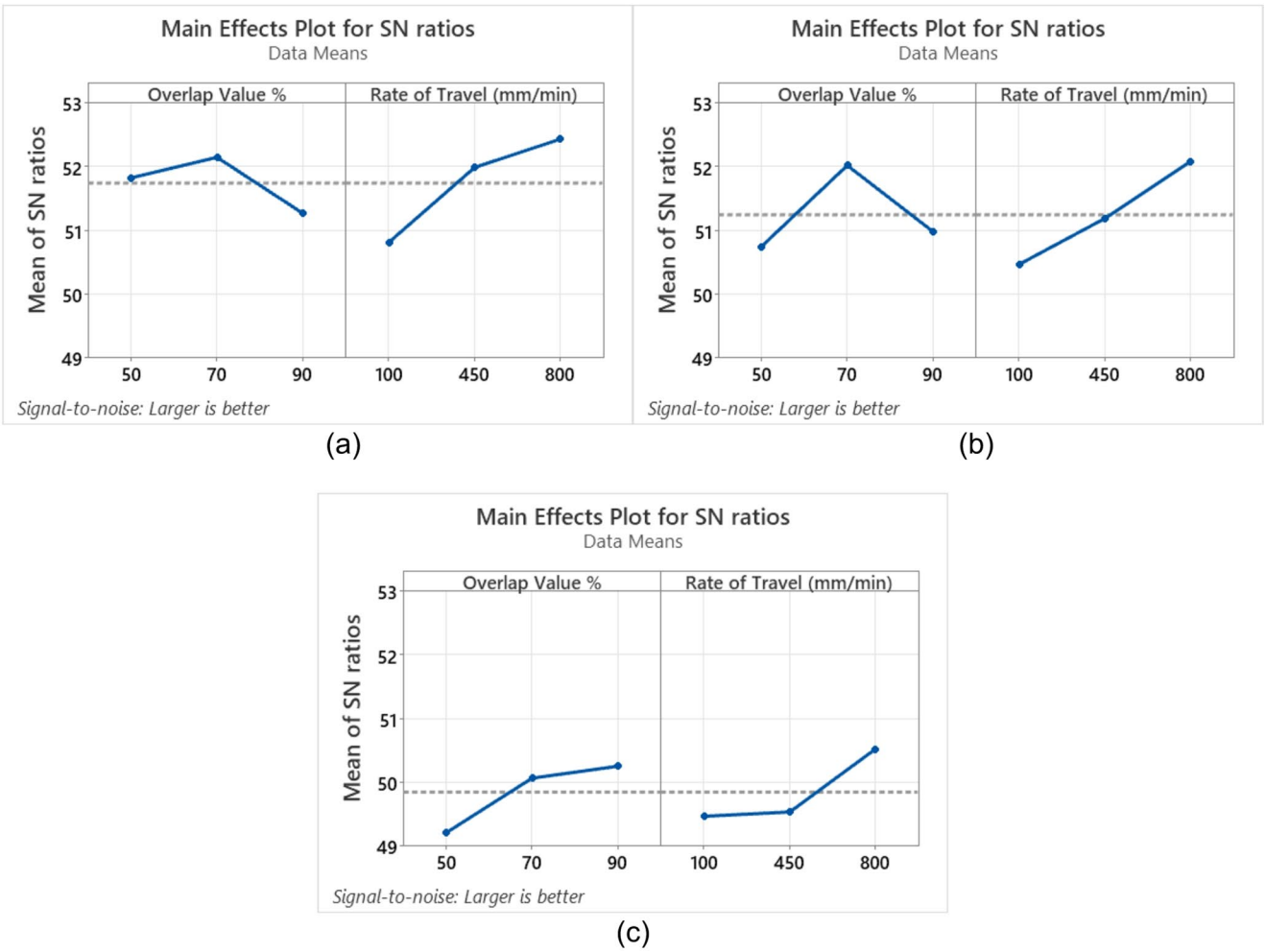


Fig. 7 Plot of SN Ratios for average microhardness (**a**) top deposition, (**b**) middle deposition (**c**) substrate below deposition

52.4, suggesting that travel rate has a more pronounced effect on deposition performance. These results highlight the rate of travel as the dominant parameter influencing the top deposition hardness. Rapid cooling at the top layer leads to equiaxed grain formation, which is highly sensitive to changes in travel rate. Faster travel rates reduce heat input, promoting finer grains and higher hardness.

In the middle deposition the overlap value peaks at 70% (52.1). For the rate of travel, a progressive increase in SN ratio is observed, rising from 50.8 at 100 mm/min to 52.0 at 450 mm/min, and reaching the highest at 52.4 at 800 mm/min. These findings affirm that an overlap value of 70% and a travel rate of 800 mm/min are the optimal parameters for achieving superior robustness and process stability in middle deposition layers. The middle layer exhibits cellular grains formed under moderate thermal gradients. These structures are relatively stable, explaining the low sensitivity to parameter changes. This outcome is consistent with theoretical expectations and prior studies, which suggest that intermediate layers in DLMD experience more uniform thermal dissipation and reduced sensitivity to process fluctuations. The presence of elongated cellular grains in this region, as observed in Fig. 8(c), supports this interpretation. The structures form under moderate cooling rates and are less influenced by minor changes in heat input.

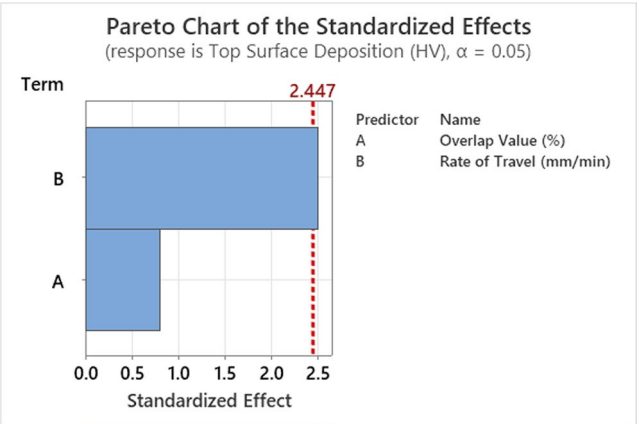


Fig. 8 Pareto chart average microhardness top deposition

For the substrate below deposition, the SN ratio analysis shows a gradual improvement with increasing overlap values, rising from 49.2 at 50% to 50.4 at 90%, reflecting incremental gains in stability. Conversely, the rate of travel has a more significant effect, with the SN ratio climbing sharply to 50.6 at 800 mm/min. This suggests that both parameters especially travel rate have a noticeable influence on process stability and microhardness consistency in the substrate region. The microhardness does show variation, even if not statistically significant. The substrate region exhibits columnar grain growth, a result of steep thermal gradients during solidification. Increased overlap enhances material consolidation in this zone, which contributes to improved microhardness. While travel rate influences the cooling rate and thermal input, its effect is moderated by the substrate's inherent thermal insulation, leading to a less pronounced impact compared to upper deposition layers. Hence, the optimal parameters for achieving average superior hardness and robustness across all deposition regions are an overlap value of 70% and a rate of travel of 800 mm/min, with the rate of travel consistently showing the most pronounced effect on performance as compare to overlap value.

Additionally, the regression equation offers valuable insights into the relationships between the predictor variables and the response variable, specifically the average microhardness across the top deposition, middle deposition, and substrate below deposition. By quantifying the influence of parameters such as overlap value and rate of travel, these equation highlights how predictors contribute to variations in average microhardness at each deposition regions. Equations (9), (10) and (11) represent the specific regression models developed for predicting the average microhardness (HV) in the top deposition, middle deposition, and substrate regions, respectively.

$$\begin{aligned} &Avg.\ Top\ Deposition\ (HV) \\ &= 383.4 - 0.561\ Overlap\ Value\ (\%) + 0.0993\ Rate\ of\ Travel\ (mm/\mathrm{min}) \end{aligned} \tag{9}$$

$$\begin{aligned} &Avg.\ Middle\ Deposition\ (HV) \\ &= 314 + 0.21\ Overlap\ Value\ (\%) + 0.0927\ Rate\ of\ Travel\ (mm/\mathrm{min}) \end{aligned} \tag{10}$$

$$\begin{aligned} &Avg.\ Substrate\ Below\ Deposition\ (HV) \\ &= 225.3 + 0.903\ Overlap\ Value\ (\%) + 0.0542\ Rate\ of\ Travel\ (mm/\mathrm{min}) \end{aligned} \tag{11}$$

The top surface region exhibits contrasting behavior due to the interaction of its parameter coefficients. The negative overlap value coefficient (-0.561) indicates that higher overlap percentages decrease microhardness, while the positive rate of travel coefficient (0.0993) improves it. The negative overlap effect may be attributed to increased heat input and slower cooling at higher overlap values. The positive rate of travel effect shows that higher travel rates reduce heat input per unit length, increasing cooling rates and which enhances hardness. This combination of opposing effects creates a skewed sensitivity in the top surface. While the layer responds positively to adjustments in rate of travel, the negative impact of the overlap value diminishes its overall robustness. This highlights the top surface layer exhibits high sensitivity to the rate of travel but faces challenges from the opposing effects of overlap value, making it less robust overall.

In the middle deposition region, both the overlap value (0.21) and rate of travel (0.0927) have positive coefficients in the regression model, indicating that increases in either parameter lead to microhardness improvement. Since the effects of these two parameters are complementary, they collectively enhance the robustness of the middle deposition region. This balance is indicative of the intermediate position, where thermal dissipation is more controlled compared to the top deposition. The positive overlap value effect suggests that higher overlap percentages contribute to uniform heat distribution and material consolidation, improving microstructural refinement and hardness. The positive rate of travel effect supports consistent cooling and reduces excessive heat input. This synergy between the two parameters makes the middle layer less sensitive to extreme variations resulting in enhanced robustness and ease of optimization in a more predictable and stable response to changes in deposition parameters.

The substrate below deposition demonstrates a markedly different sensitivity profile, characterized by a strong positive overlap value coefficient (0.903) and a minor positive rate of travel coefficient (0.0542). These values indicate that the substrate responds more strongly to overlap value adjustments than to changes in travel rate. The dominance of the overlap value reflects the substrate's dependence on cumulative heat input and material consolidation. A higher overlap percentage contributes significantly to substrate hardness by increasing material density and uniformity during the deposition process. The minor effect of rate of travel suggests that changes in cooling rate have limited influence on the substrate, likely because the substrate's position beneath deposition material buffers it from rapid thermal gradients. The substrate's response to parameter changes is gradual, with relatively low sensitivity compared to the top surface or middle layer. This reflects the thermal insulation provided by the upper layers, resulting in a more uniform but less dynamic cooling environment.

The revised ANOVA analysis in Table 5 indicates that rate of travel is a statistically significant predictor of top deposition, with a P-value of 0.047. A P-value less than the conventional significance level of 0.05 ($\alpha = 0.05$) suggests that the observed relationship between rate of travel and top deposition is unlikely to be due to random chance. This implies that modifying the rate of travel has a meaningful and consistent impact on the response variable, likely

Table 5 Revised ANOVA average microhardness top deposition

Source	Degree of freedom	Sum of squares	Mean squares	F-Value	*P*-Value
Regression	2	7999.4	3999.7	3.45	0.101
Overlap Value (%)	1	756.4	756.4	0.65	0.450
Rate of Travel (mm/min)	1	7243.1	7243.1	6.25	0.047
Residual	6	6956.6	1159.4		
Total	8	14956.0			

Table 6 Revised ANOVA average microhardness middle deposition

Source	Degree of freedom	Sum of squares	Mean squares	F-Value	*P*-Value
Regression	2	6423.1	3211.6	0.73	0.522
Overlap Value (%)	1	107.2	107.2	0.02	0.881
Rate of Travel (mm/min)	1	6315.9	6315.9	1.43	0.277
Residual	6	26558.8	4426.5		
Total	8	32981.9			

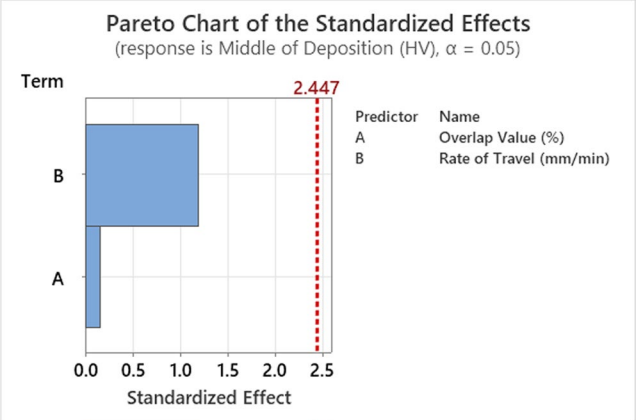


Fig. 9 Pareto chart average microhardness top deposition

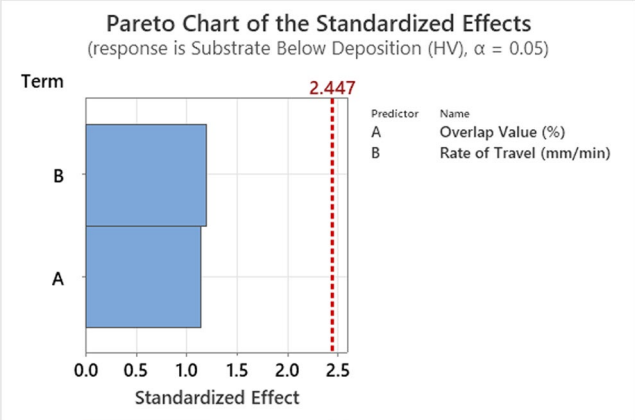


Fig. 10 Pareto chart average microhardness middle deposition

through its effects on heat input, cooling rates, and microstructural characteristics. The regression model for the top deposition layer demonstrates reliable and actionable predictive power, with an R^2 value of 0.535 indicating that over half of the variation in microhardness can be explained by the selected process parameters which particularly the statistically significant influence of travel rate. This aligns well with the observed equiaxed grain structures formed under rapid cooling, which are known to enhance hardness due to increased grain boundary density. However, limitations remain. The model does not account for other potentially influential factors such as laser power fluctuations, powder flow consistency, or ambient thermal conditions, which may introduce variability not captured in the current analysis. Additionally, the sample size and experimental scope may constrain generalizability, suggesting that while the model is effective for guiding optimization within the tested range, further refinement is needed for broader application.

This relationship is further supported by the Pareto chart (Fig. 9), where the rate of travel bar extends beyond the significance threshold ($\alpha = 0.05$), represented by the red dashed line at 2.447. The significance threshold marks the point at which the predictor's standardized effect is strong enough to be considered statistically significant. Since the Rate of Travel's effect exceeds this threshold, it is clear that it has a substantial and statistically significant impact on deposition. In contrast, the overlap value does not have a significant effect on top deposition, with a P-value of 0.450. A P-value greater than 0.05 indicates that there is no statistically significant relationship between overlap value and the response variable. This is further supported by the Pareto chart, where the overlap value bar does not extend beyond the significance threshold.

For middle deposition, the revised ANOVA analysis reveals that both overlap value and rate of travel exhibit minimal effects on the middle deposition as tabulated in Table 6 below.

The overlap value has a p-value of 0.881, which is far above the significance threshold, indicating that it does not have a meaningful effect on the response variable. Similarly, the rate of travel has a p-value of 0.277, which also exceeds the 0.05 threshold, confirming that it does not significantly influence the middle deposition. The Pareto chart (Fig. 10) visually reinforces the findings. In this case, both overlap value and rate of travel have bars that do not exceed this threshold. This indicates that neither predictor has a statistically significant effect on the middle deposition. The regression model for the middle deposition layer exhibits weak predictive power, with an R^2 value of 0.195 indicating that only a small portion of the variation in microhardness is explained by the selected process parameters. This limited performance reflects the statistical insignificance of both overlap value and travel rate, as confirmed by high P-values in the ANOVA results. The microstructural characteristics

of this region was dominated by elongated cellular grains formed under moderate and stable thermal gradients which further reduce sensitivity to parameter changes, resulting in more uniform hardness profiles. Limitations to consider include the narrow range of input variables, which may overlook other influential factors such as melt pool dynamics or interlayer thermal accumulation. Additionally, the relatively small sample size and inherent thermal buffering in the middle layer constrain the model's responsiveness, suggesting that refinement through expanded parameter sets or alternative modeling approaches is necessary to improve predictive accuracy.

Finally, the statistical analysis presented in Table 7 provides a view of the influence of process parameters on average microhardness for the substrate below deposition while Fig. 11 shows Pareto chart respectively.

The findings from the ANOVA and the Pareto chart both suggest that the model and the individual parameters exhibit limited predictive power. Similarly, both overlap value (p-value: 0.298) and rate of travel (p-value: 0.276) fail to reach the 0.05 significance threshold, suggesting that these parameters do not have a meaningful effect on the response. The Pareto chart in Fig. 11 further supports these findings. Neither both exceed the significance threshold of 2.447 ($\alpha = 0.05$), reinforcing that neither factor has a statistically significant impact. The regression model for the substrate below the deposition demonstrates moderate reliability for trend interpretation, with an R^2 value of 0.313 indicating that approximately 31.3% of the variation in microhardness is explained by the selected process parameters. While neither overlap value nor travel rate reached statistical significance in the ANOVA results, the model still captures meaningful directional trends. This is supported by microstructural observations, where columnar grain growth and thermal insulation in the substrate region contribute to a more gradual response to process changes. However, limitations must be considered. The model's predictive strength is constrained by the substrate's inherent thermal buffering, which dampens the effect of surface-level parameter adjustments. Additionally, the exclusion of other influential variables such as laser energy density, substrate preheating, or interfacial bonding conditions may limit the model's comprehensiveness. As such, while the model is useful for identifying general trends, it requires refinement for precise prediction and broader applicability.

Table 7 Revised ANOVA average microhardness substrate below deposition

Source	Degree of freedom	Sum of squares	Mean squares	F-Value	*P*-Value
Regression	2	4118	2059	1.37	0.324
Overlap Value (%)	1	1958	1958	1.30	0.298
Rate of Travel (mm/min)	1	2160	2160	1.43	0.276
Residual	6	9039	1506		
Total	8	13,157			

Although the ANOVA results for the middle and substrate below deposition layers did not reach statistical significance, this outcome is itself informative. It demonstrates that overlap value and travel rate exert minimal influence on hardness in deeper regions, where microstructural evolution is dominated by thermal buffering and grain morphology. This stability highlights the layer-dependent sensitivity of the deposition process. The parameter adjustments are most effective at the top surface, while deeper layers respond primarily to intrinsic thermal gradients. Such findings are valuable for process optimization, as they prevent unnecessary parameter tuning in regions where hardness is inherently insensitive, and instead direct attention to the surface layer where mechanical performance more effective.

Further trend analysis was conducted by plotting surface plots shown in Fig. 12to provide a comprehensive overview of the parameter effects. For top deposition, optimal conditions are visually represented by the blue regions on the contour plot, highlighting favorable parameter ranges. The hardness of the middle deposition layer shows an upward trend, though the effects are less pronounced compared to the top surface. The impact is moderate. This suggests that the middle layer's thermal and structural evolution is less responsive to parameter adjustments, reflecting a more stabilized energy transfer and microstructural transformation compared to the surface layer. Meanwhile, the substrate below deposition exhibits the least sensitivity to parameter variations, reflecting a gradual and more stabilized response. This behavior is likely due to thermal gradients and energy transfer intensity at greater depths due to heat flux [5].

The hardness at the top surface can be explained by rapid cooling and localized thermal gradients during deposition, which accelerate phase transformations. Variations in hardness across the layers reflect a dynamic heat treatment phenomenon [43–45], where factors such as overlap values and travel rates modulate thermal input, facilitating microstructural refinement. The top surface likely experiences rapid transformation due to near-instantaneous cooling, leading to a high dislocation density and increased yield strength [46]. This morphology resulting in higher microhardness values. The experimental data confirm this trend, with the top layer consistently exhibiting the highest hardness under optimized travel rate conditions. In contrast, the middle layer shows elongated cellular grains formed under moderate thermal gradients, leading to slightly lower hardness. The substrate region, dominated by columnar grains due to steep directional heat flow, demonstrates reduced hardness due to larger grain size and lower boundary density. This integrated

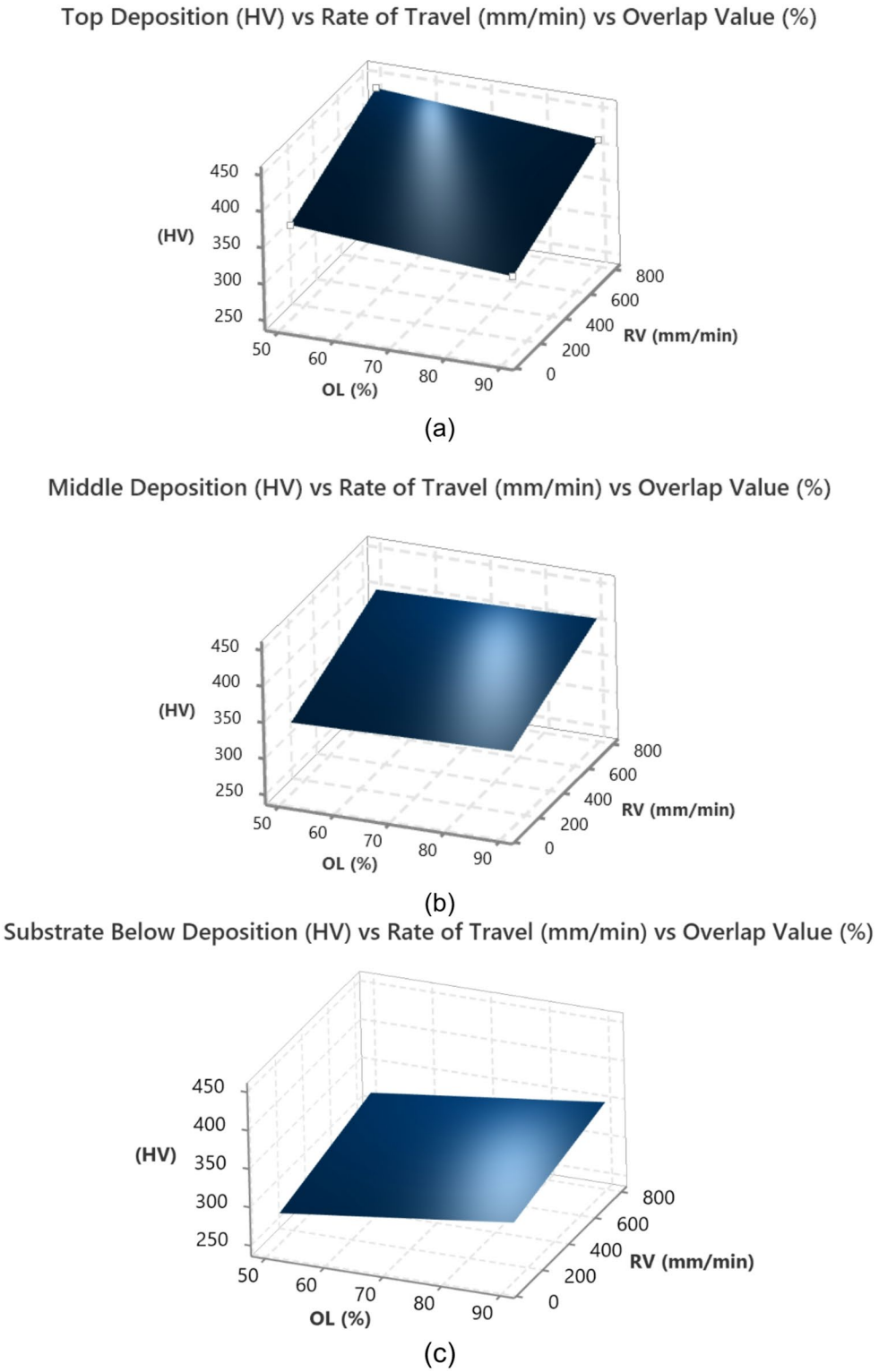


Fig. 11 Summary of surface plot: (**a**) top deposition (**b**) middle deposition (**c**) substrate below deposition

analysis reinforces the role of thermal conditions and grain morphology in determining mechanical performance.

The optimization analysis identified 70% overlap and a travel rate of 800 mm/min as the most effective parameters for maximizing hardness at the top deposition layer. To verify this prediction, experimental trials were conducted under these conditions. The measured hardness values closely matched the expected results, confirming the optimization outcome as shown in Table 8.

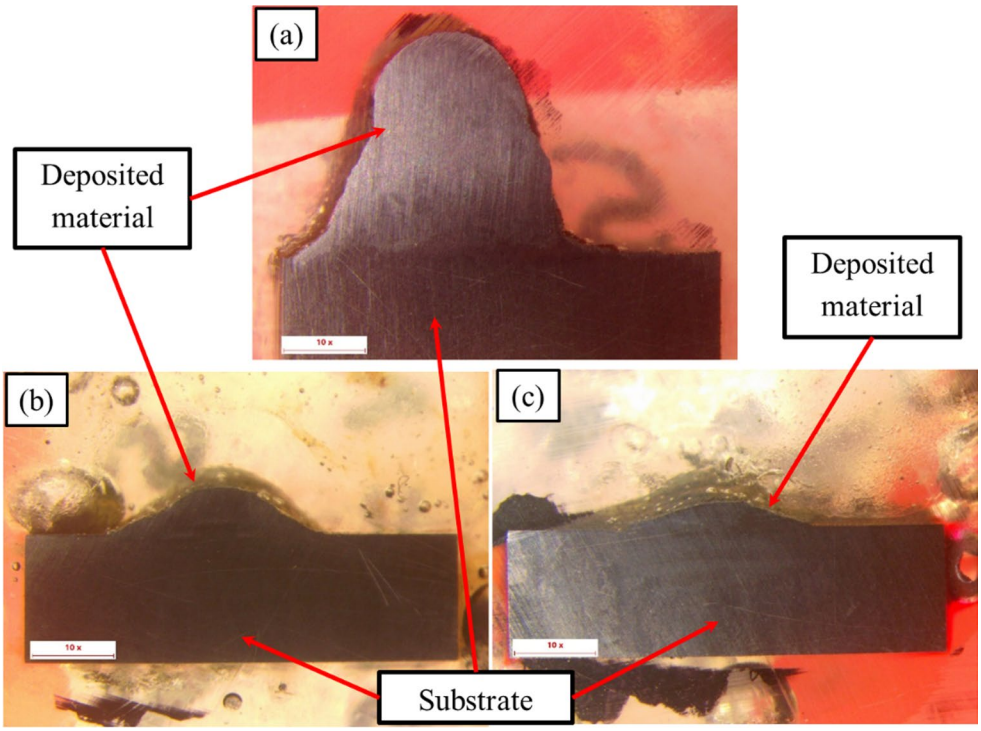
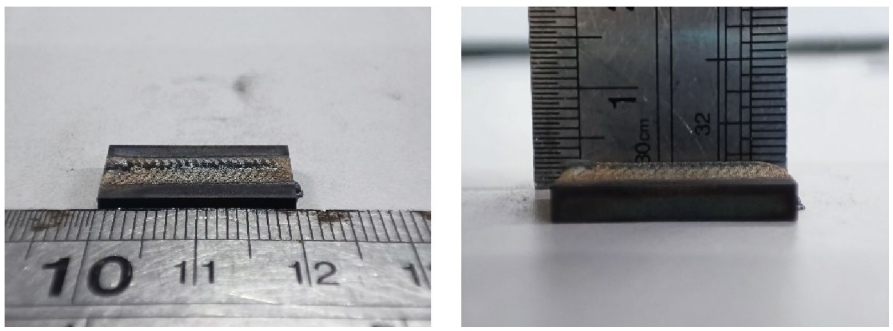


Fig. 12 Cross sectional view of deposited material with parameter OL=50% and (**a**) RV=100mm/min (**b**) RV=450mm/min (**c**) RV=800mm/min

Table 8 Verification of Optimum Parameters (Top Layer Hardness)

Parameter	OL values (%)	RV (mm/min)	Measured Hardness (HV)	Expected Hardness (HV)
Optimum	70	800	412	~410



For the middle deposition and substrate regions, although the S/N analysis suggested optimum parameter sets, their effects were not statistically significant relative to the study's objective. This reinforces that parameter adjustments exert the greatest influence at the top layer, where rapid cooling and equiaxed grain formation drive hardness enhancement.

Optical analysis was subsequently performed, as shown in Fig. 13, where the cross-sectional images illustrate how variations in travel speed (RV) affect the deposition geometry, with the overlap value (OL) maintained at 50%. The three examined travel speeds are 100 mm/min, 450 mm/min and 800 mm/min demonstrate distinct variations in deposition height and width while associated its thermal effects. At a low travel speed of 100 mm/min, the deposition profile is characterized by increased height and small variance of average width due to greater material accumulation and higher heat input, leading to deeper material melting and a taller profile. Medium travel speed (450 mm/min) achieves

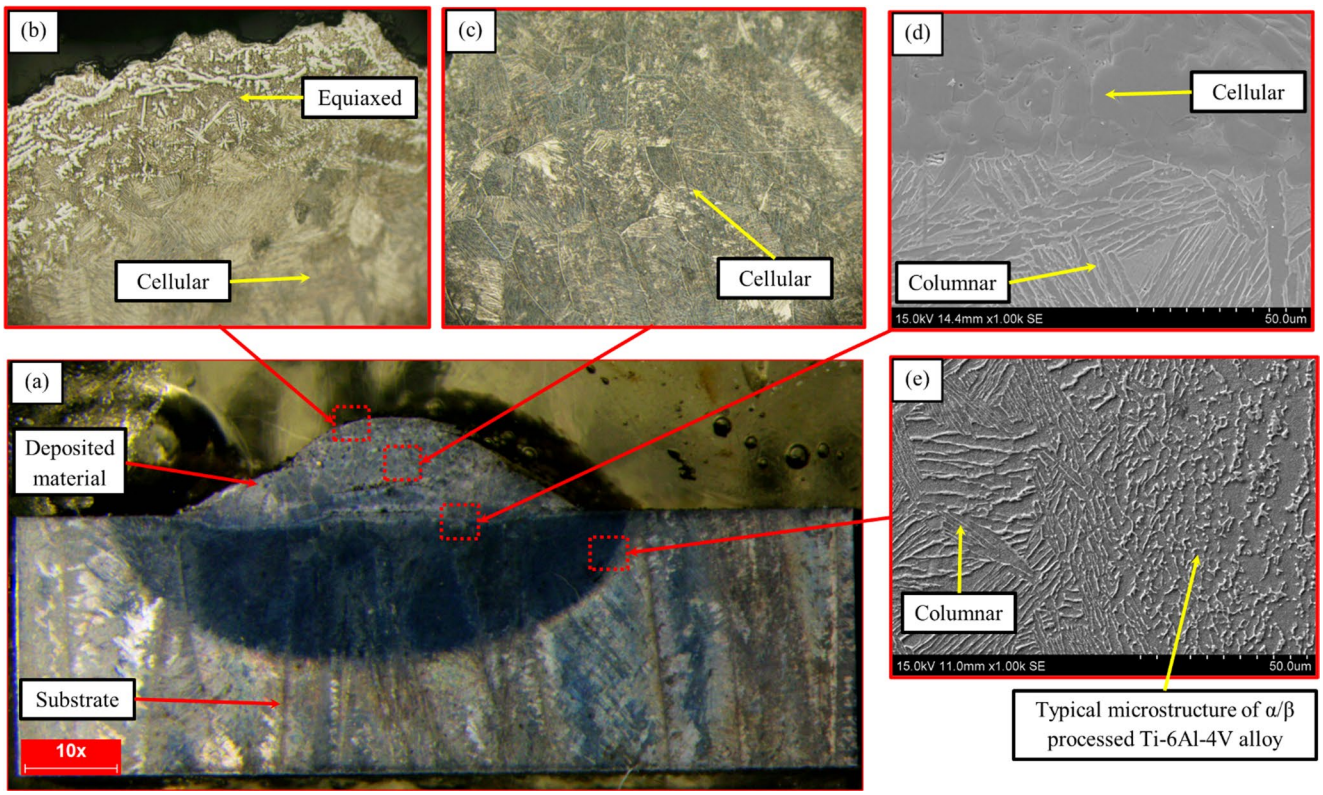


Fig. 13 Images of deposited material (**a**) microscopic view of the cross sectioned sample (**b**) microstructure at top region using optical microscope (**c**) microstructure at middle region using optical microscope(**d**) microstructure at the border between deposited material and substrate using SEM analysis (**e**) microstructure at border between HAZ and substrate using SEM analysis

a balanced profile with moderate height and average width, reflecting a stable equilibrium between heat input and material deposition rate, which minimizes extremes in thermal gradients and promotes finer microstructures. At the highest travel speed of 800 mm/min, the deposition becomes shallower due to reduced material deposition and faster cooling rates, resulting in a thinner layer with rapid solidification contributing to finer grain structures.

Figure 8 presents the images obtained from the cross-section of the deposited material, showcasing both optical microscope images and SEM images. These images provide a detailed view of the microstructural characteristics, highlighting the differences in grain structure. The observed microstructure in the deposition layers reveals a combination of columnar, cellular, and equiaxed dendrites, each influenced by thermal gradients and solidification rates during the DLMD process. The top section of the deposited material, exposed to the surrounding environment and shielding gas, undergoes rapid heat dissipation, significantly reducing the solidification time and suppressing the directional growth of columnar dendrites, leading to an equiaxed structure as shown in Fig. 8(b). A low thermal gradient to solidification rate promotes the transition to equiaxed growth [47]. The high cooling rate enhances heterogeneous nucleation, resulting in a larger number of small grains that grow independently in different directions, forming an equidimensional structure as mentioned by previous researchers [30, 48, 49]. Equiaxed grains exhibit superior microhardness attributed to their fine grain size and elevated dislocation density.

Figure 8(c) illustrates the formation of cellular structures in the middle region of the DLMD process, governed by unique thermal and solidification conditions. In this region, the cooling rate is slower compared to the top. This intermediate cooling rate promotes the growth of elongated cellular structures by providing sufficient time for their development [50]. The temperature gradient reflects a balance between heat conduction and solidification rates, favoring the formation of cellular structures aligned perpendicular to the solidification front [26]. While these structures exhibit a slightly lower microhardness compared to equiaxed grains, their morphology aids in resisting crack propagation, thus contributing to the mechanical robustness of the material. The border between the deposited material and the substrate in Fig.8(d) shows a mix of cellular and columnar structures due to the steep temperature gradient caused by heat conduction into the substrate. These gradient drives

directional solidification, with cellular grains forming near the deposited material where the cooling rate is moderate. The higher gradient in the substrate promotes the growth of columnar grains aligned with the heat flow. Such alignment, a result of directional solidification, enhances both strength and hardness [26].

Last but not least, the formation of columnar structures predominantly in the substrate HAZ region shown in Fig. 134(e). In this region, the cooling rate is slower compared to the middle and top regions, allowing the material sufficient time to solidify in a columnar pattern. The steep temperature gradient shown near the substrate facilitates directional heat flow away from the molten pool, promoting the alignment of elongated columnar grains parallel to the heat flow direction [51]. This alignment ensures a denser and more uniform microstructure, bolstering the material's hardness and strength as compare to the typical grain of Ti-6Al-4 V.

The findings of this study have direct relevance to industries that rely on Ti-6Al-4 V components, particularly aerospace, biomedical, and high-performance tooling sectors, where surface integrity and wear resistance are critical. The demonstrated improvement in microhardness suggests enhanced durability and load-bearing capacity for parts subjected to cyclic stress or abrasive environments. This is especially valuable in aerospace applications, where Ti-6Al-4 V is widely used for turbine blades, structural brackets, and landing gear components due to its high strength-to-weight ratio and corrosion resistance [52]. By establishing a controlled oscillation strategy and validating its effect through Taguchi and ANOVA methods, this research provides an initial parameter screening under fixed conditions for tailoring surface properties without compromising dimensional accuracy. However, the study was based on a relatively small sample size, and environmental factors such as ambient temperature fluctuations, powder flow variability, and laser stability during deposition may introduce result variability. These factors, while controlled to the extent possible, could influence microstructural evolution and hardness outcomes, suggesting that further validation under industrial-scale conditions is warranted.

4 Conclusion

This study provides an initial parameter screening to explore how overlap value (OL) and travel rate (RV) affect microhardness and microstructural features in DLMD. From single-track deposition trials, the combination of 70% overlap and 800 mm/min travel rate emerged as the most effective setting for enhancing hardness at the surface layer, where process sensitivity is greatest. Statistical assessment using Taguchi analysis and ANOVA indicated travel rate as the dominant factor influencing hardness at the top region, while responses in the middle and substrate below deposition layers were comparatively weak, with low R^2 values and non-significant p-levels. Regression analysis indicated differing levels of sensitivity across the deposition regions. The top layer exhibited the greatest responsiveness to changes in travel rate, reflected in an R^2 value of 0.535. In contrast, the middle and substrate below deposition layers showed weaker predictive strength, with R^2 values of 0.195 and 0.313 respectively, suggesting reduced sensitivity to parameter variation. Microstructural observations revealed equiaxed grains at the surface, cellular structures in the middle, and columnar grains in the substrate below deposition, consistent with the hardness distribution across layers. These findings highlight that parameter adjustments are most effective at the surface, where mechanical performance can be most readily improved, while deeper regions remain relatively insensitive due to intrinsic thermal gradients and buffering. This layer-dependent behavior provides useful guidance for process control, directing optimization efforts toward the top layer and avoiding unnecessary tuning in regions where hardness is inherently stable. The absence of statistical significance in the ANOVA results for the middle and substrate below deposition layers reinforces this interpretation, showing that overlap value and travel rate exert minimal influence on hardness in deeper regions. These values indicate directional tendencies rather than strong statistical effects, reflecting the constraints of sample size and replication.

Acknowledgements This research is fully supported by Universiti Teknologi Malaysia under grant No: Q.J130000.3824.24H00. Their support has made this important research viable and effective.

Funding Open Access funding enabled and organized by CAUL and its Member Institutions

Data availability Not applicable.

Declarations

Ethics approval Not applicable.

Consent to participate Not applicable.

Consent for publication Not applicable.

Generative AI and AI-assisted technologies in the writing process During the preparation of this work the author(s) used Microsoft Copilot services in order to improve language style of writing. After using this tool/service, the author(s) reviewed and edited the content as needed

and take(s) full responsibility for the content of the publication.

Conflict of interest The authors declare no competing interests.

Open Access This article is licensed under a Creative Commons Attribution 4.0 International License, which permits use, sharing, adaptation, distribution and reproduction in any medium or format, as long as you give appropriate credit to the original author(s) and the source, provide a link to the Creative Commons licence, and indicate if changes were made. The images or other third party material in this article are included in the article's Creative Commons licence, unless indicated otherwise in a credit line to the material. If material is not included in the article's Creative Commons licence and your intended use is not permitted by statutory regulation or exceeds the permitted use, you will need to obtain permission directly from the copyright holder. To view a copy of this licence, visit http://creativecommons.org/licenses/by/4.0/.

References

1. Jadhav A, Jadhav VS (2022) A review on 3D printing: an additive manufacturing technology. Mater Today Proc 62(Part 4, 2022):2094–2099. https://doi.org/10.1016/j.matpr.2022.02.558
2. Lalegani Dezaki M, Serjouei A, Zolfagharian A, Fotouhi M, Moradi M, Ariffin MKA, Bodaghi M (2022) A review on additive/subtractive hybrid manufacturing of directed energy deposition (DED) process. Advanced Powder Materials 1:4. https://doi.org/10.1016/j.apmate.2022.100054
3. Errico V, Posa P, Mazzarisi M, Angelastro A, Campanelli SL (2022) Effects of laser-deposited maraging steel on L-PBF 316L component. Metals 12:10. https://doi.org/10.3390/met12101669
4. ISO/ASTM 59000:2021 (2021) International Organization for Standardization/American Society for Testing and Materials. Additive manufacturing – General principles – Terminology. International Organization for Standardization, Geneva, Switzerland
5. Moradi M, Hasani A, Pourmand Z, Lawrence J (2021) Direct laser metal deposition additive manufacturing of Inconel 718 superalloy: statistical modelling and optimization by design of experiments. Opt Laser Technol 144(March):107380. https://doi.org/10.1016/j.optlastec.2021.107380
6. Moradi M, Kornokar K, Nematzadeh F, Mostaan H, Meiabadi S, Demers V, Lawrence J (2023) Microstructural and mechanical investigation on fiber laser welding of S500MC steel. Sādhanā 48:1. https://doi.org/10.1007/s12046-023-02079-2
7. Moradi M, Pourmand Z, Hasani A, Karami Moghadam M, Sakhaei AH, Shafiee M, Lawrence J (2022) Direct laser metal deposition (DLMD) additive manufacturing (AM) of Inconel 718 superalloy: elemental, microstructural and physical properties evaluation. Optik 259(March):169018. https://doi.org/10.1016/j.ijleo.2022.169018
8. Pragana JPM, Sampaio RFV, Bragança IMF, Silva CMA, Martins PAF (2021) Hybrid metal additive manufacturing: a state–of–the-art review. Adv Ind Manuf Eng 2(October 2020):100032. https://doi.org/10.1016/j.aime.2021.100032
9. Pellizzari M, Zhao Z, Bosetti P, Perini M (2022) Optimizing direct laser metal deposition of H13 cladding on CuBe alloy substrate. Surf Coat Technol 432(October 2021):128084. https://doi.org/10.1016/j.surfcoat.2022.128084
10. Wu D, Tian J, Liao M, Zhao M, Liu G (2024) Study on the effect of variable laser power on residual stress distribution in laser directed energy deposition of Ti6Al4V. CIRP J Manufact Sci Technol 55(October):322–332. https://doi.org/10.1016/j.cirpj.2024.10.011
11. Rauch M, Hascoët J-Y, Mallaiah M (2020) Repairing Ti-6Al-4V aeronautical components with DED additive manufacturing. MATEC Web of Conferences, 321, 03017. https://doi.org/10.1051/matecconf/202032103017
12. Mahamood RM, Akinlabi ET, Akinlabi S (2015) Laser power and scanning speed influence on the mechanical property of laser metal deposited titanium-alloy. Lasers Manuf Mater Process 2(1):43–55. https://doi.org/10.1007/s40516-014-0003-y
13. Rezaee Hajideh M, Farahani M (2023) Direct laser metal deposition cladding of IN718 on DIN 1.2714 tool steel reinforced by the SiC nanoparticles. J Mater Res Technol 23:2020–2030. https://doi.org/10.1016/j.jmrt.2023.01.107
14. Ali N, Tomesani L, Ascari A, Fortunato A (2022) Fabrication of thin walls with and without close loop control as a function of scan strategy via direct energy deposition. Lasers Manuf Mater Process 9(1):81–101. https://doi.org/10.1007/s40516-022-00164-8
15. Mazzarisi M, Angelastro A, Latte M, Colucci T, Palano F, Campanelli SL (2023) Thermal monitoring of laser metal deposition strategies using infrared thermography. J Manuf Process 85:594–611. https://doi.org/10.1016/j.jmapro.2022.11.067
16. Svetlizky D, Zheng B, Steinberg DM, Schoenung JM, Lavernia EJ, Eliaz N (2022) The influence of laser directed energy deposition (DED) processing parameters for Al5083 studied by central composite design. J Mater Res Technol 17:3157–3171. https://doi.org/10.1016/j.jmrt.2022.02.042
17. Srivastava D, Chang ITH, Loretto MH (2000) The optimisation of processing parameters and characterisation of microstructure of direct laser fabricated TiAl alloy components. Mater Des 21(4):425–433. https://doi.org/10.1016/s0261-3069(99)00091-6
18. Piscopo G, Atzeni E, Saboori A, Salmi A (2023) An overview of the process mechanisms in the laser powder directed energy deposition. Appl Sci (Switzerland) 13:1. https://doi.org/10.3390/app13010117
19. Singh A, Kapil S, Das M (2020) A comprehensive review of the methods and mechanisms for powder feedstock handling in directed energy deposition. Addit Manuf 35:101388. https://doi.org/10.1016/j.addma.2020.101388
20. Pinkerton AJ (2015) Advances in the modeling of laser direct metal deposition. J Laser Appl 27(S1):S15001. https://doi.org/10.2351/1.4815992
21. Guo M, Huang G, Xi L, Dai D, Gu D (2022) Effects of laser printing parameters on molten pool formation, microstructure evolution and mechanical properties of laser directed energy deposition of difficult-to-process tungsten heavy-alloy. CIRP J Manuf Sci Technol 39:401–413. https://doi.org/10.1016/j.cirpj.2022.09.002
22. Weaver JS, Heigel JC, Lane BM (2022) Laser spot size and scaling laws for laser beam additive manufacturing. J Manuf Process 73:26–39. https://doi.org/10.1016/j.jmapro.2021.10.053
23. Tapoglou N, Clulow J, Patterson A, Curtis D (2022) Characterisation of mechanical properties of 15-5PH stainless steel manufactured through direct energy deposition. CIRP J Manuf Sci Technol 38:172–185. https://doi.org/10.1016/j.cirpj.2022.04.004
24. Odermatt AE, Dorn F, Ventzke V, Kashaev N (2022) Coaxial laser directed energy deposition with wire of thin-walled duplex stainless steel parts: process discontinuities and their impact on the mechanical properties. CIRP J Manuf Sci Technol 37:443–453. https://doi.org/10.1016/j.cirpj.2022.02.019
25. Fujishima M, Oda Y, Ashida R, Takezawa K, Kondo M (2017) Study on factors for pores and cladding shape in the deposition processes of Inconel 625 by the directed energy deposition (DED) method. CIRP J Manuf Sci Technol 19:200–204. https://doi.org/10.1016/j.cirpj.2017.04.003

26. Baek GY, Shin GY, Lee KY, Shim DS (2019) Mechanical properties of tool steels with high wear resistance via directed energy deposition. Metals 9:3. https://doi.org/10.3390/met9030282
27. Wang Z, Lu G, Lu H, Zhang H, Xu X, Luo K, Lu J (2025) Tailoring laser directed energy deposited Ti6Al4V titanium alloy for superior and isotropic mechanical properties by interlayer pause — intertrack pause cooling strategy. Addit Manuf 97:104595. https://doi.org/10.1016/j.addma.2024.104595
28. Yellup JM (1995) Laser cladding using the powder blowing technique. Surf Coat Technol 71(2):121–128. https://doi.org/10.1016/0257-8972(94)01010-G
29. Ujjwal K, Raman RKS, Kumar Das A (2024) Role of arc weaving strategies in the fabrication of thick-walled 4043 aluminium alloy components through directed energy deposition process. CIRP J Manuf Sci Technol 52(May):12–25. https://doi.org/10.1016/j.cirpj.2024.05.016
30. Xiang S, Luan H, Wu J, Yao KF, Li J, Liu X, Tian Y, Mao W, Bai H, Le G, Li Q (2019) Microstructures and mechanical properties of CrMnFeCoNi high entropy alloys fabricated using laser metal deposition technique. Journal of Alloys and Compounds 773:387–392. https://doi.org/10.1016/j.jallcom.2018.09.235
31. Muslim T, Karagoz T, Kurama S, Sezer P, Yazici OF, Ozkok R (2023) Laser metal deposition of 17–4 PH stainless steel: geometrical, microstructural, and mechanical properties investigation for structural applications. CIRP J Manuf Sci Technol 41:69–79. https://doi.org/10.1016/j.cirpj.2022.12.010
32. Bidare P, Jiménez A, Hassanin H, Essa K (2022) Porosity, cracks, and mechanical properties of additively manufactured tooling alloys: a review. Adv Manuf 10(2):175–204. https://doi.org/10.1007/s40436-021-00365-y
33. Li Z, Sui S, Ma X, Tan H, Zhong C, Bi G, Clare AT, Gasser A, Chen J (2022) High deposition rate powder- and wire-based laser directed energy deposition of metallic materials:a review. International Journal of Machine Tools and Manufacture. https://doi.org/10.1016/j.ijmachtools.2022.103942
34. Udroiu R, Braga IC, Nedelcu A (2019) Evaluating the quality surface performance of additive manufacturing systems: methodology and a material jetting case study. Materials 12:6. https://doi.org/10.3390/ma12060995
35. Thompson SM, Bian L, Shamsaei N, Yadollahi A (2015) An overview of direct laser deposition for additive manufacturing; Part I: transport phenomena, modeling and diagnostics. Addit Manuf 8:36–62. https://doi.org/10.1016/j.addma.2015.07.001
36. Cheng J, Xing Y, Dong E, Zhao L, Liu H, Chang T, Wan J (2022) An overview of Laser Metal Deposition for cladding: defect formation mechanisms, defect suppression methods and performance improvements of laser-cladded layers. Materials. https://doi.org/10.3390/ma15165522
37. Shi Y, Gong S, Xu H, Yang G, Qiao J, Wang Z, Qi B (2023) Electron beam metal additive manufacturing: defects formation and in-process control. J Manuf Process 101(February):386–431. https://doi.org/10.1016/j.jmapro.2023.06.013
38. Svetlizky D, Das M, Zheng B, Vyatskikh AL, Bose S, Bandyopadhyay A, Schoenung JM, Lavernia EJ, Eliaz N (2021) Directed energy deposition (DED) additive manufacturing: physical characteristics, defects, challenges and applications. Mater Today 49(October):271–295. https://doi.org/10.1016/j.mattod.2021.03.020
39. Piscopo G, Iuliano L (2022) Current research and industrial application of laser powder directed energy deposition. Int J Adv Manuf Technol 119(11–12):6893–6917. https://doi.org/10.1007/s00170-021-08596-w
40. Gabor T, Yun H, Akin S, Kim KH, Park JK, Jun MBG (2022) Continuous coaxial nozzle designs for improved powder focusing in direct laser metal deposition. J Manuf Process 83(September):116–128. https://doi.org/10.1016/j.jmapro.2022.08.039
41. Aversa, A., Carrozza, A., Marchese, G., Felicioni, S., De Chirico, M., Lombardi,M., … Fino, P. (2022). Productivity Enhancement in Directed Energy Deposition: The Oscillating Scanning Strategy Approach. *Metals and Materials International*, (0123456789). https://doi.org/10.1007/s12540-022-01356-9
42. Francis Z (2017) *The Effects of Laser and Electron Beam Spot Size in Additive Manufacturing Processes*. *Ph.D. Dissertation*. Carnegie Mellon University. Retrieved from https://search.proquest.com/docview/1906683857?fromunauthdoc=true&pq-origsite=gscholar%0Ahttp://repository.cmu.edu/dissertations/909
43. Yuan J, Wang H, Cheng X, Gao H, Li Z (2024) Materials Science & Engineering A effect of heat treatment on microstructure and mechanical anisotropy of. Mater Sci Eng A 916(October):147364. https://doi.org/10.1016/j.msea.2024.147364
44. Ren B, Zhang M, Chen C, Wang X, Zou T, Hu Z (2017) Effect of heat treatment on microstructure and mechanical properties of Stellite 12 fabricated by laser additive manufacturing. J Mater Eng Perform 26(11):5404–5413. https://doi.org/10.1007/s11665-017-2984-0
45. Liu Z, Zhao D, Wang P, Yan M, Yang C, Chen Z, Lu Z (2022) Additive manufacturing of metals: microstructure evolution and multistage control. J Mater Sci Technol 100:224–236. https://doi.org/10.1016/j.jmst.2021.06.011
46. Mostafaei A, Ghiaasiaan R, Ho I, Strayer S, Chang K, Shamsaei N, Yeh A (2023) Progress in materials science additive manufacturing of nickel-based superalloys: a state-of-the-art review on process-structure-defect-property relationship. Prog Mater Sci 136(March):101108. https://doi.org/10.1016/j.pmatsci.2023.101108
47. Wang T, Zhu YY, Zhang SQ, Tang HB, Wang HM (2015) Grain morphology evolution behavior of titanium alloy components during laser melting deposition additive manufacturing. J Alloys Compd 632:505–513. https://doi.org/10.1016/j.jallcom.2015.01.256
48. Henry S, Cle F, Wagnie J, Kurz W (1999) Epitaxial laser metal forming: analysis of microstructure formation. 271:232–241
49. Zhao Z, Wang C, Yu Q, Song L, Yang G, Zhang J (2022) New β-type Ti-Zr-V-Nb alloys used for laser-based direct energy deposition: design, microstructure, and properties. Mater Charact. https://doi.org/10.1016/j.matchar.2022.111917
50. Baek GY, Shin GY, Lee EM, Shim DS, Lee KY, Yoon HS, Kim MH (2017) Mechanical characteristics of a tool steel layer deposited by using direct energy deposition. Met Mater Int 23(4):770–777. https://doi.org/10.1007/s12540-017-6442-1
51. Luo X, Yang C, Fu ZQ, Liu LH, Lu HZ, Ma HW, Wang Z, Li DD, Zhang LC, Li YY (2021) Achieving ultrahigh-strength in beta-type titanium alloy by controlling the melt pool mode in Selective Laser Melting. Mater Sci Eng A. https://doi.org/10.1016/j.msea.2021.141731
52. Gradl PR (2021) *Principles of Directed Energy Deposition for Aerospace Applications*. *Drive AM Industry Connect W.M. Keck Center for 3D Innovation*. https://doi.org/10.13140/RG.2.2.10504.75527

Publisher's note Springer Nature remains neutral with regard to jurisdictional claims in published maps and institutional affiliations.